Chemical Science

ROYAL SOCIETY OF CHEMISTRY

EDGE ARTICLE

View Article Online
View Journal | View Issue

Check for updates

Cite this: *Chem. Sci.*, 2025, **16**, 14366

All publication charges for this article have been paid for by the Royal Society of Chemistry

Received 5th May 2025
Accepted 3rd July 2025

DOI: 10.1039/d5sc03240g

rsc.li/chemical-science

Extrinsic gating of the rotary direction of a light-driven molecular motor by dynamic boronic acid–diol complexation†

Zi-Jian Chen,[a] Hsiu-Feng Lu,[b] Chun-Wei Chiu,[a] Yi-Hung Liu,[a] Chao-Ping Hsu *[bc] and Jye-Shane Yang *[ad]

Chiral sterically overcrowded alkenes are potential candidates for artificial light-driven rotary molecular motors (LRMMs), which perform a full 360° unidirectional rotation around the C═C bond through a series of photochemical and thermal isomerization processes. However, the majority of the reported LRMMs adopt an intrinsic chirality (*i.e.*, an integration of the chirality center with the photoresponsive unit), which hampers the effective gating of their rotary direction through chirality switching. Herein, we report a new sterically overcrowded alkene equipped with a boronic acid receptor for dynamic covalent bonding with chiral vicinal diols, enabling it to function as an extrinsic chirality-based LRMM. The dynamic boronic acid-chiral diol B–O bonding not only implements the extrinsic chirality to induce a helical preference in the alkene backbone but also facilitates chirality switching through diol exchange to reverse the rotation direction. This work demonstrates that dynamic covalent bonding for extrinsic chirality implementation is an effective strategy for designing direction-switchable LRMMs, paving the way for more sophisticated molecular motors with applications in complex (bio)environments.

Introduction

The precision and efficiency with which nature controls the transmission and directionality of molecular motion to perform work have inspired the development of artificial molecular machines capable of performing designated mechanical functions at the molecular level.[1–3] Among these, light-driven rotary molecular motors (LRMMs) undergo light-powered unidirectional 360° rotation, overcoming random thermal motions.[4–17] Feringa and co-workers pioneered the use of chiral sterically overcrowded alkenes for designing LRMMs, where unidirectional rotation around the central C═C bond leverages the inherent helicity preference arising from the interplay between the chirality center and the alkene backbone.[4–10] This 360° unidirectional rotation generally comprises four alternating strokes of light and heat with two energetically uphill photo-*E*/*Z*-isomerization (PEZ) steps and two energetically downhill thermal helix inversion (THI) steps. The direction of rotation is determined during the THI steps, in which the metastable helical form produced *via* PEZ flips its helicity to generate the stable helical form. For instance, in the LRMM illustrated in Fig. 1a, the *S*-configuration chirality center of the α-carbonyl carbon confers a conformational preference for *M* helicity, resulting in clockwise rotation. Beyond overcrowded alkenes, LRMMs based on chiral imines,[11,12] hemithioindigos[13,14] oxindoles,[15] and barbituric acids[16] have also been developed. Potential applications of LRMMs include controlling the movement of microscale objects on functional surface,[18] regulating dynamic supramolecular self-assemblies,[19,20] influencing chemical equilibrium,[21] opening cell membranes,[22–24] facilitating transmembrane ion transport,[25] creating artificial muscles,[26,27] deforming macroscopic materials,[28–30] and governing stem cell differentiation.[31]

One defining features of biological rotary motors is their ability to switch direction.[32,33] However, designing direction-switchable LRMMs remains challenging because it requires effective configuration switching at the chirality center[6,9] or altering the rotational axis,[34] unlike chemically-powered molecular motors whose directionalities could be switched on demand by flipping the chirality of input reagents.[35] To date, only two examples of chirality switching in LRMMs have been reported. The earlier example (Fig. 1a) involves base-catalyzed epimerization of an α-carbonyl chirality center intrinsically integrated into the sterically overcrowded alkene backbone.[6] In contrast to this configurational inversion of intrinsic chirality (IC), the second example (Fig. 1b) utilizes the enantiomers of

---

[a] Department of Chemistry, National Taiwan University, Taipei, 10617, Taiwan. E-mail: jsyang@ntu.edu.tw

[b] Institute of Chemistry, Academia Sinica, Taipei, 11529, Taiwan. E-mail: cherri@sinica.edu.tw

[c] Division of Physics, National Center for Theoretical Sciences, Taipei, 106319, Taiwan

[d] Center for Emerging Material and Advanced Devices, National Taiwan University, Taipei, 10617, Taiwan

† Electronic supplementary information (ESI) available. CCDC 2294942 and 2294943. For ESI and crystallographic data in CIF or other electronic format see DOI: https://doi.org/10.1039/d5sc03240g

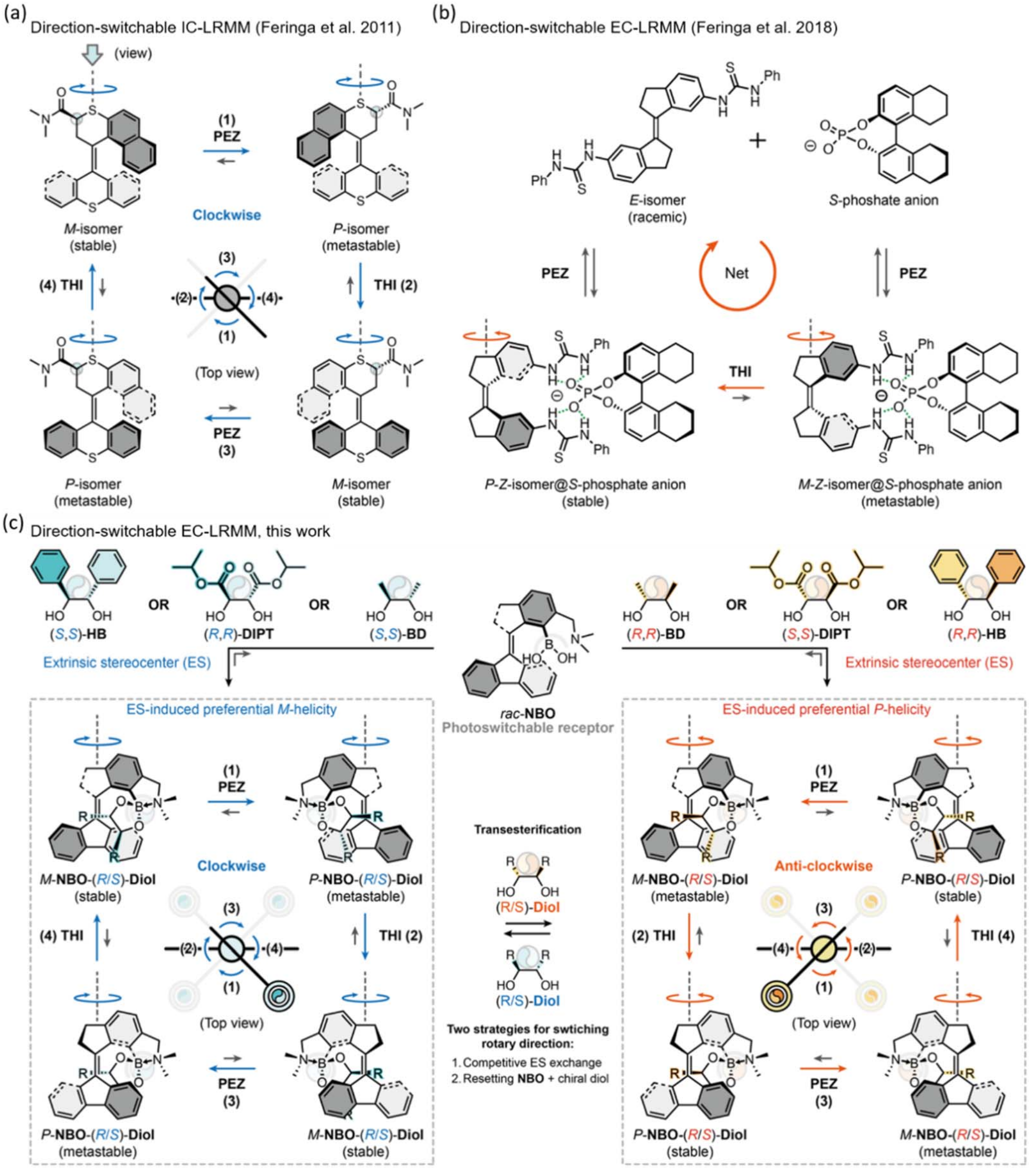

Fig. 1 Direction-switchable light-driven rotary molecular motors of sterically overcrowded alkenes: (a and b) the previously reported systems based on intrinsic chirality (IC) (a) and noncovalently bonded extrinsic chirality (EC) (b), and (c) this work based on dynamically covalent bonded extrinsic chirality (EC). The unidirectional rotation is driven by light-powered photo-*E*/*Z*-isomerization (PEZ) of the stable isomer to generate the metastable isomer (step 1), followed by thermal helix inversion (THI) to form the stable isomer (step 2). A full 360° rotation is achieved with further consecutive PEZ (step 3) and THI (step 4) for (a) and (c), but only the PEZ for (b). Switching the directionality of LRMMs between clockwise and anticlockwise rotation was performed by base-catalyzed epimerization of the metastable isomer for (a), by using phosphate ligand of opposite chirality for (b), and by transesterification of the boronate ester for (c).

external chirality (EC) for direction switching.[9] Specifically, it employs a stiff-stilbene scaffold equipped with thiourea groups, which serve as receptors for noncovalently binding with chiral phosphate ligands in the *Z* form but not in the *E* form. The three-step isomerization cycle for a full 360° unidirectional rotation involves the association and dissociation of the chiral ligands, potentially reducing motor efficiency. While the sense of rotation can be altered by using a phosphate ligand of opposite chirality, further experiments to demonstrate direction-switching were not conducted.

Here, we present a new strategy for a direction-switchable LRMM based on dynamic covalent bonding. Specifically, the boronic acid group in a sterically overcrowded alkene (**NBO**) acts as a receptor for binding with chiral vicinal diols *via* the well-documented dynamic covalent B–O bonding (Fig. 1c).[36–38] Additionally, the presence of an amino group adjacent to the boronic acid enables the formation of an N → B dative bond upon boronic acid–diol complexation.[39] Our results demonstrate that the chiral **NBO-Diol** complexes function as LRMMs and show that chirality exchange *via* diol substitution leads to a rotary direction switch.

Results and discussion

Molecular design and synthesis

Structural helicity and chirality center-induced helical preference are fundamental features of overcrowded alkene-based LRMMs.[4–10] The *ortho*-substituted stiff-stilbene scaffold in **NBO** fulfils the requirement for helicity,[7,40–42] while the chiral diols (EC) can be readily incorporated by forming cyclic boronate esters with the *ortho*-aminomethyl phenylboronic group in the rotor unit (the upper half) of **NBO**. Additionally, the symmetric lower half (the stator unit) of **NBO** was designed based on the concept of Feringa's second-generation LRMMs to simplify the structural and energetic profile for the rotation cycles.[5] We also anticipated that N → B dative bonding would accelerate the esterification process and stabilize the resulting boronic ester,[39] thereby facilitating the anchoring of EC. Owing to the dynamic covalent nature of the bonding, direction switching of the resulting **NBO-Diol** system can be achieved *via* a thermodynamically controlled exchange of the chiral diol.

Scheme 1 outlines the synthesis of **NBO**, starting from commercially available 1-indanone though intermediates **1–8**. A key step involving the Barton–Kellogg reaction to construct the overcrowded alkene framework of **NBO** was carried out according to procedures developed by Feringa and coworkers.[43] The diol recognition site in **NBO** was constructed from **6** in three steps: (1) nitrile reduction using DIBAL-H, (2) reductive amination of the resulting formyl group with dimethylamine, and (3) borylation at the bromo-substituted carbon using *n*-butyl lithium.

Diol-induced helical preference

We first employed the C_2-symmetric vicinal diol (*S*,*S*)-hydrobenzoin (**HB**) to investigate the helical preference of **NBO-Diol** complexes (Fig. 2a). This was accomplished by monitoring the spectral evolutions in ^{1}H and ^{11}B NMR (in CD_3CN) and circular dichroism (CD, in CH_3CN) spectra (Fig. 2b–d). NMR signal assignments were validated using a series of 2D NMR spectra (Fig. S1 and S2†). Before diol complexation, the ^{1}H NMR spectrum of **NBO** exhibits anisochronous resonances (Fig. 2b(i)) for the benzylic protons (H_{23} and $H_{23'}$) at 3.5 and 3.9 ppm, indicating a slow THI nature (*i.e.*, racemization). Additionally, the singlet signal for the dimethylamino group (H_{24} and $H_{24'}$) at 2.3 ppm reflects rapid rotation about the C–N bond. The ^{11}B NMR spectrum of **NBO** shows a single resonance at 22.2 ppm (Fig. 2c(i)), consistent with a trigonal geometry at the boron center and the absence of N → B coordination.[44] Furthermore, the CD spectrum is silent, confirming the racemic nature of **NBO** (Fig. 2d). Upon addition of (*S*,*S*)-**HB**, the ^{11}B NMR spectrum exhibits a significant upfield shift from 22.2 ppm to 12.8 ppm, indicating the formation of the boronic acid–diol complex **NBO**-(*S*,*S*)-**HB** with an N → B dative bond and a tetrahedral geometry at the boron center (Fig. 2c(ii)).[44] Formation of the N → B dative bond is further supported by the anisochronous signals for the benzylic protons (H_{23} and $H_{23'}$) and the methyl protons (H_{24} and $H_{24'}$) (Fig. 2b(ii)). The driving force for N → B bond formation arises from the increased Lewis acidity of the boron atom in the 5-membered cyclic boronate ester.[39] Although both *P* and *M* helical forms of **NBO**-(*S*,*S*)-**HB** are initially formed comparable amounts (Fig. 2b(i)–(iii)), heating the solution to 80 °C for four hours results in one form becoming predominant, with a stable: metastable ratio of 95 : 5, revealing the EC effect of (*S*,*S*)-**HB** on the helical preference of **NBO** (Fig. 2b(iv)). The difference in Gibbs free energy between the two helical forms induced by the EC effect was determined as 2.0 ± 0.4 kcal mol^{-1} at 80 °C through van't Hoff analysis (Fig. S3, Tables S1 and S2†), which agrees with the observed 95 : 5 equilibrium ratio. The EC effect also causes different shielding (H_9) and deshielding (H_6) of the aromatic protons in the metastable and stable forms. Surprisingly, the benzylic protons (H_{23} and $H_{23'}$) and methyl protons (H_{24} and $H_{24'}$) of the metastable form exhibit a larger downfield shift ($\Delta\delta = 0.59$ ppm) compared to the stable form ($\Delta\delta = 0.53$ ppm), indicating stronger N → B bonding in the metastable form. The

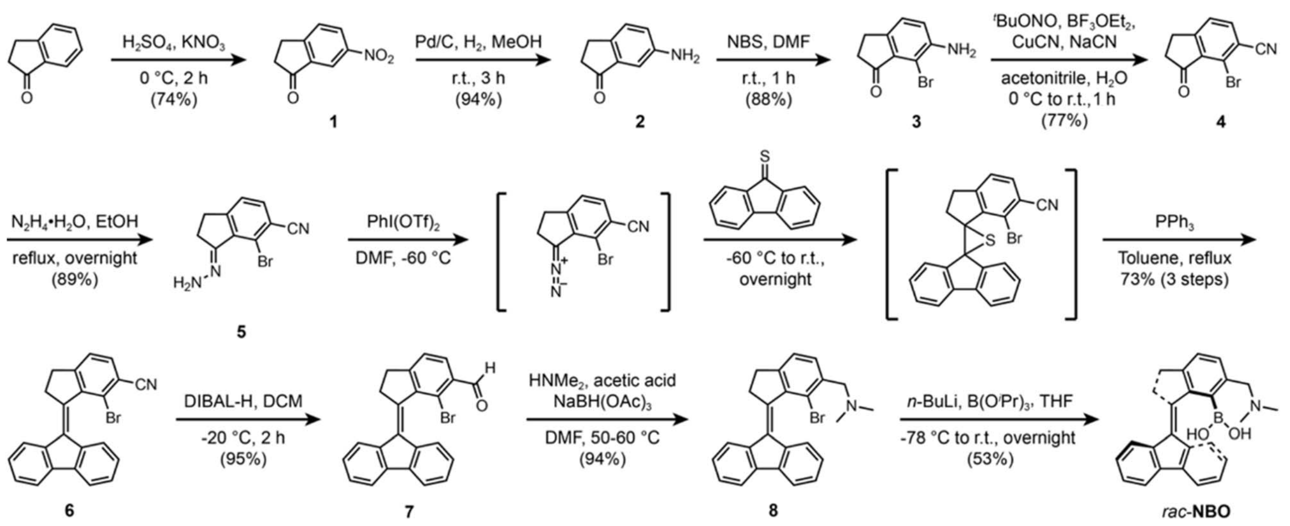

Scheme 1 Synthesis of NBO.

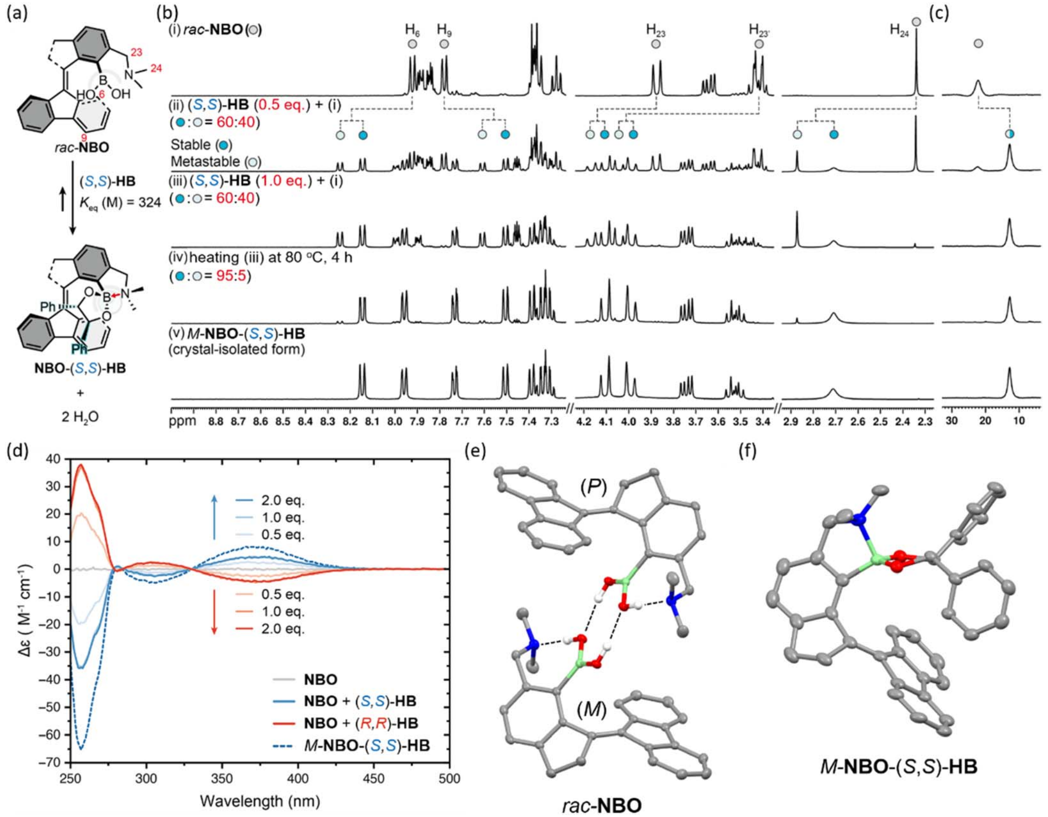

Fig. 2 (a) Esterification between *rac*-NBO and (*S*,*S*)-hydrobenzoin (HB). The equilibrium constant (K_{eq}) for esterification was determined according to the integration of the ^{1}H NMR signals of the species involved.[45] (b)–(d) Spectral evolutions in (b) ^{1}H NMR (400 MHz, CD_3CN), (c) ^{11}B NMR (128 MHz, CD_3CN), and (d) CD spectra that reflect the HB-induced helical preference of NBO. (e) The crystal structure of *rac*-NBO, displaying a pair of helical enantiomers assembled by hydrogen bonding (dashed lines). (f) The crystal structure of *M*-NBO-(*S*,*S*)-HB.

corresponding CD spectra show a positive Cotton effect for the long-wavelength absorption band (λ_{max} ∼375 nm). For comparison, the enantiomer (*R*,*R*)-**HB** produced mirrored CD spectra (Fig. 2d). Since the chiral diol precursors are CD-silent in this spectral region (Fig. S4†), these results clearly demonstrate that chiral diol complexation induces a helical conformational preference in **NBO**.

The X-ray crystal structures of **NBO** and **NBO**-(*S*,*S*)-**HB** provide insights into the stable form present in acetonitrile solution. The crystal of **NBO** consists of both *P* and *M* helical isomers, paired through hydrogen bonding between the trigonal planar boronic acid moieties (Fig. 2e). The O–B–O bond angle is 120.06°, characteristic of trigonal geometry, with an average B–O bond length of 1.36 Å. Additionally, the nitrogen atoms form hydrogen bonds with the boronic hydroxyl groups without establishing an N → B dative bond, consistent with observations in acetonitrile solution. In contrast, the crystal structure of **NBO**-(*S*,*S*)-**HB** reveals only the *M* form with an N → B dative bond and a tetrahedral boron center (Fig. 2f). Two independent molecules are present in the crystal, showing slight conformational differences in the overcrowded alkene scaffold. Their N → B dative bond lengths are 1.757 Å and 1.779 Å, while the O–B–O bond angles are 108.31° and 108.75°, with average B–O bond lengths of 1.44 Å and 1.43 Å. Dissolving the crystals in CD_3CN produces a ^{1}H NMR spectrum corresponding to the stable form of **NBO**-(*S*,*S*)-**HB**, confirming that **NBO**-(*S*,*S*)-**HB** preferentially adopts *M* helicity in both solution and solid state. Accordingly, *M*-**NBO**-(*S*,*S*)-**HB** exhibits a positive CD signal at λ_{max} ∼375 nm, while the opposite CD signal observed for **NBO**-(*R*,*R*)-**HB** confirms a preference for *P* helicity.

The correlation between helical preference and the Cotton effect observed for **NBO-HB** complexes extends to other chiral diols, such as 2,3-butanediol (**BD**) and diisopropyl tartrate (**DIPT**). The formation of the **NBO-Diol** complexes was evidenced by evolution in ^{1}H NMR and CD spectra (Fig. 3) and mass spectrometry (Fig. S5†). As shown in Fig. 3a and b, (*S*,*S*)-**BD** induces a positive Cotton effect at 375 nm, indicating a preference for *M* helicity in **NBO**-(*S*,*S*)-**BD** (stable : metastable = 70 : 30, see Fig. S6† for full spectrum). Conversely, the mirrored CD spectrum induced by (*R*,*R*)-**BD** reflects a preference for *P* helicity. Importantly, even the reduced steric bulkiness of **BD** compared to **HB** maintains the helical preference for **NBO**. Similarly, (*R*,*R*)-**DIPT**, which shares the same absolute configuration as (*S*,*S*)-**BD** and (*S*,*S*)-**HB**, induces *M* helicity in **NBO**, with an extent of chirality induction (stable : metastable = 92 : 8, see Fig. S7† for full spectrum) comparable to that of **HB** (stable : metastable = 95 : 5) (Fig. 3c and d). The opposite Cotton effect induced by (*S*,*S*)-**DIPT** further confirms the helicity dependence on the absolute configuration of chiral diols. These findings demonstrate that chiral diols can effectively induce a helical

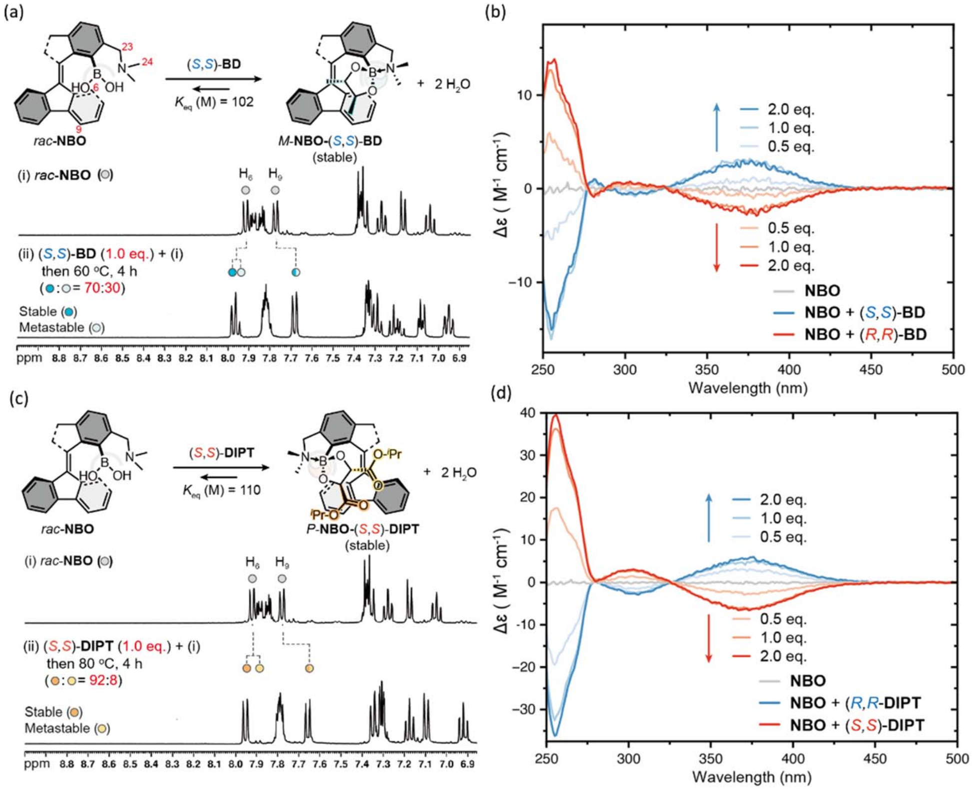

Fig. 3 (a) and (b) The formation of **NBO-BD** LRMM monitored by (a) ^{1}H NMR (400 MHz, CD_3CN) and (b) CD spectra (solvent: CH_3CN). (c) and (d) The formation of **NBO-DIPT** LRMM monitored by (c) ^{1}H NMR (400 MHz, CD_3CN) and (d) CD spectra (solvent: CH_3CN).

preference upon complexation with **NBO**. Furthermore, the helicity of **NBO-Diol** systems is dictated by the absolute configuration of the diols, positioning them as promising candidates for EC-LRMMs.

Light-driven unidirectional rotation of NBO-Diol systems

The pure *M*-**NBO**-(*S*,*S*)-**HB** LRMM obtained by dissolving the corresponding crystal in acetonitrile serves as an ideal candidate for evaluating the performance of **NBO-Diol** as an EC-LRMM. Upon irradiation of *M*-**NBO**-(*S*,*S*)-**HB** with 419 nm light at ambient temperature, the photostationary state (PSS_{419nm}) exhibits an *M*-to-*P* ratio of 25 : 75, accompanied by inverted CD signals (Fig. 4a). This corresponds to the step-1 rotation (PEZ (1)) shown in Fig. 1c. Subsequent heating of the PSS_{419nm} sample to 80 °C results in a significant recovery of the initial CD signals, indicating the THI from the metastable *P* form back to the stable *M* form (*i.e.*, step 2 in Fig. 1c). The *M*-to-*P* ratio shifts to 96 : 4 after this step (denoted as $THI_{80°C}$). These combined steps of PEZ and THI accomplish a clockwise 180° rotation of rotator about the C=C bond. Repeating the same PEZ and THI steps enables a complete 360° unidirectional rotation, thereby establishing the EC-LRMM behavior of **NBO**-(*S*,*S*)-**HB**.

For practical operation, boronic acid-diol complexation should be readily formed and displaced by simple mixing of **NBO** and chiral diols in solutions without additional purification. In this regard, we evaluated the PEZ and THI behaviors of **NBO**-(*S*,*S*)-**HB** (*M* : *P* = 95 : 5) generated *in situ* by mixing *rac*-

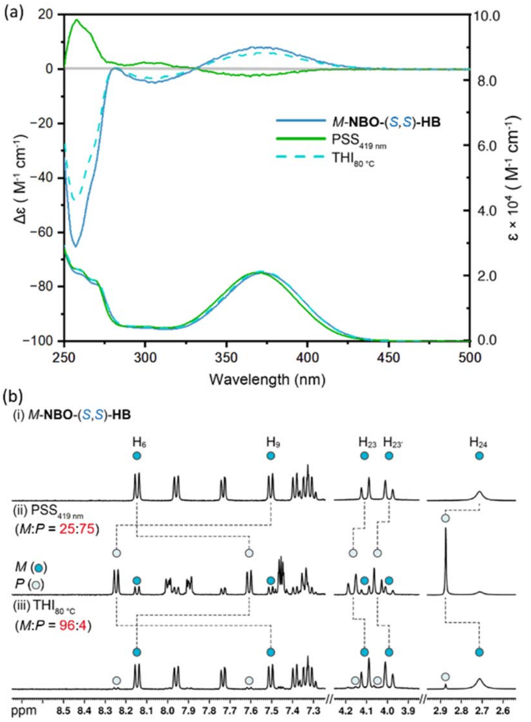

Fig. 4 (a) CD (top) and UV-vis (bottom) spectra (in CH_3CN) and (b) ^{1}H NMR spectra (400 MHz, CD_3CN) of *M*-**NBO**-(*S*,*S*)-**HB** before and after irradiation with 419 nm light at room temperature (PSS_{419nm}), and after heating at 80 °C for 4 hours ($THI_{80°C}$).

NBO with (*S*,*S*)-**HB**, and compared them to those of pure *M*-**NBO**-(*S*,*S*)-**HB** samples obtained from single crystals. As shown in Fig. 5a and b, their PEZ and THI behaviors are indistinguishable from those of the pure *M*-**NBO**-(*S*,*S*)-**HB**, displaying identical compositions at both $\mathrm{PSS}_{419\mathrm{nm}}$ ($M:P = 25:75$) and $\mathrm{THI}_{80^\circ\mathrm{C}}$ ($M:P = 95:5$). The evolution in the corresponding CD spectra also mirrored closely to those of *M*-**NBO**-(*S*,*S*)-**HB** samples. This trial confirms the *in situ* generation of **NBO**-(*S*,*S*)-**HB** complexes is an effective approach to prepare functional **NBO-Diol** molecular motors.

Next, we evaluated the unidirectional rotation performance of LRMMs **NBO**-(*S*,*S*)-**BD** ($M:P = 70:30$) and **NBO**-(*S*,*S*)-**DIPT** ($M:P = 8:92$) prepared *in situ* in acetonitrile. As shown in Fig. 5c–f, the stable-to-metastable ratios at $\mathrm{PSS}_{419\mathrm{nm}}$ are 43 : 57 for **NBO**-(*S*,*S*)-**BD** and 44 : 56 for **NBO**-(*S*,*S*)-**DIPT**. After the THI step, these ratios shift to 70 : 30 and 92 : 8, respectively. These results demonstrate that both **NBO-Diol** systems function as EC-LRMMs, although their directionality, judged by the relative stable-to-metastable ratios, is slightly reduced compared to that of **NBO**-(*S*,*S*)-**HB**. Interestingly, the rotation of **NBO**-(*S*,*S*)-**BD** is clockwise, whereas that of **NBO**-(*S*,*S*)-**DIPT** is anticlockwise (Fig. 1b). This confirms that the rotary direction of **NBO-Diol** systems can be controlled by the chirality of the diols (**BD**, **DIPT**, and **HB**). Thus, **NBO-Diol** systems successfully function as EC-LRMMs with a clockwise or anticlockwise rotary motor, depending on the diol chirality. Notably, the THI processes were found faster for **NBO**-(*S*,*S*)-**DIPT** and **NBO**-(*S*,*S*)-**BD**, compared to **NBO**-(*S*,*S*)-**HB**, which contains the bulkiest boronate group in the series (Fig. S8 and Table S3†). This suggests that dynamic ligand exchange can not only switch the direction but also fine-tune the rates of the light-driven rotation for **NBO-Diol** LRMMs.

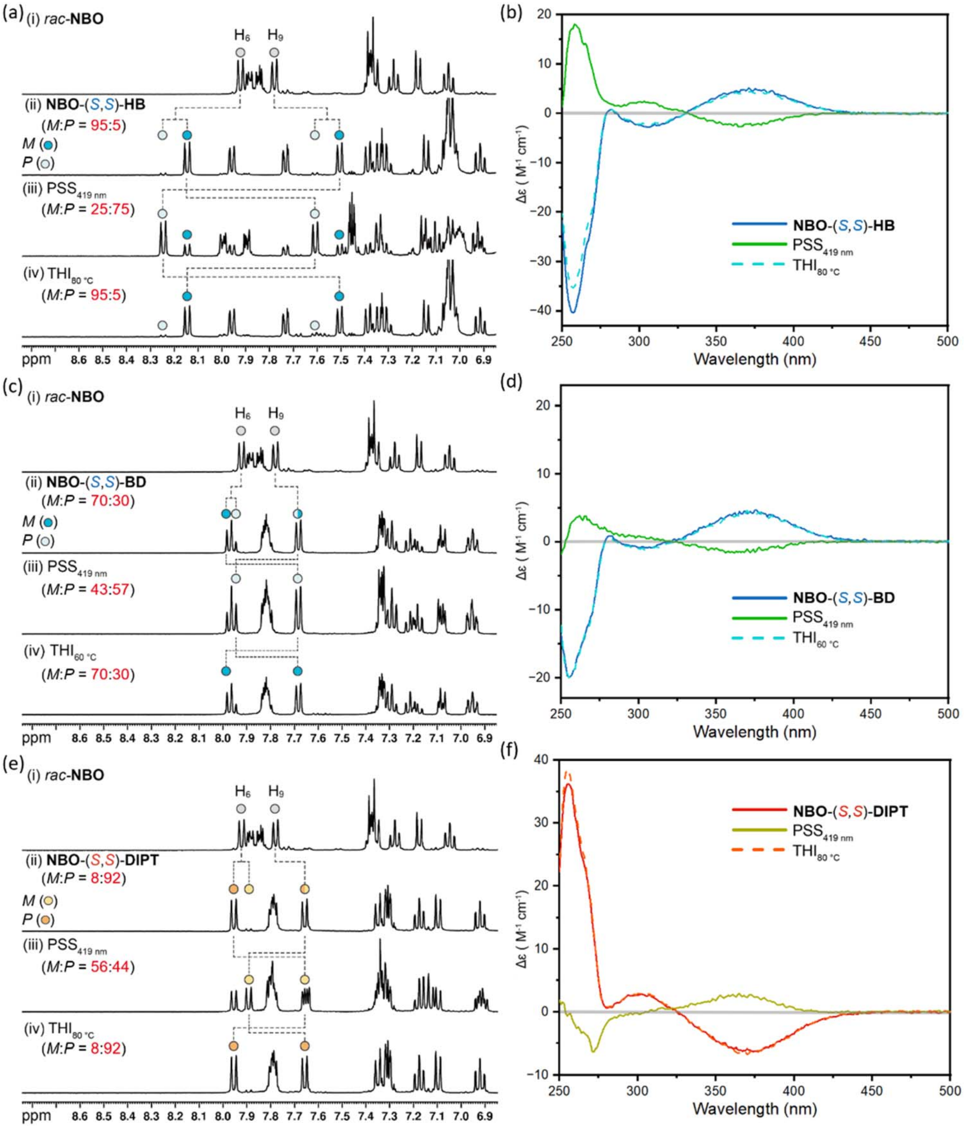

Fig. 5 Spectral changes in ^{1}H NMR (400 MHz, CD_3CN) (left) and CD (in CH_3CN) (right) spectra of *in situ* generated LRMMs **NBO**-(*S*,*S*)-**HB** (a and b), **NBO**-(*S*,*S*)-**BD** (c and d), and **NBO**-(*S*,*S*)-**DIPT** (e and f) before (ii) and after irradiation with 419 nm light at room temperature (iii) and after heating at 80 °C (60 °C for **NBO**-(*S*,*S*)-**BD**) for 4 hours (iv).

DFT calculations

To gain deeper structural insights into the THI processes of **NBO-(*S*,*S*)-HB**, DFT calculations were performed at the BMK/6-311+G**//PBE0-D3/6-31G* level of theory using an SMD CH_3CN solvation model.[46] All calculations were carried out with the Gaussian 09 program (Revision E.01).[47] The structure of *M*-**NBO-(*S*,*S*)-HB** was optimized starting from its crystal structure, and the initial structures of other configurations and THI transition states (TS) were found by rotating the C_1–B bond, rather than the $C_3{=}C_4$ bond, from the optimized structure of *M*-**NBO-(*S*,*S*)-HB.** This is because the reorientation of the boronate unit plays a more significant role than the C=C torsion during THI, which merely twists the C=C bond without breaking it. With this approach, four conformers and two THI TSs are obtained, and the TS with lower energy is reported. A comparison of the crystal structure with the optimized structures is provided in Table S4.† Fig. 6a shows the DFT-optimized structures of several representative conformations of **NBO-(*S*,*S*)-HB**, along with corresponding pictorial representations drawn according to the perspective indicated as Fig. 6b. The calculated relative Gibbs free energies of these conformations are also given. The calculations show that the orientation of the N → B dative bond could be parallel or perpendicular to the fluorene stator, referred to as the horizontal form and vertical form, respectively. Interestingly, the observed *M*-vertical form in crystals is less stable by 1.7 kcal mol^{-1} in Gibbs free energy at 298 K than the global minimum *M*-horizontal form. This prediction is consistent with the 2D ROESY spectrum of *M*-**NBO-(*S*,*S*)-HB**, which shows an NOE correlation between H_6 and $H_{24,24'}$ (Fig. S2(c)†), a spatial relationship that is much more likely to exist in the *M*-horizontal form than in the *M*-vertical form (Fig. S9†). One possible explanation is a larger steric hindrance between (*S*,*S*)-**HB** and the stator in the *M*-vertical form compared to the *M*-horizontal form. This is indicated by the distance between the C_{28} in (*S*,*S*)-**HB** and the stator face ($d_{\text{C28-S}}$), which is shorter in the *M*-vertical form ($d_{\text{C28-S}} = 3.366$ Å) than in the *M*-horizontal form ($d_{\text{C28-S}} = 3.971$ Å). Additionally, as indicated by the C_1–C_2–C_3–C_4 dihedral angle (θ), the alkene backbone shows a larger twist in the *M*-vertical form ($\theta = 43.2°$) compared to the *M*-horizontal form ($\theta = 38.6°$). Another possible explanation for the *M*-vertical form being less stable than the *M*-horizontal form is a weaker N → B bond, as indicated by a lower tetrahedral character (THC) for the boron atom in the *M*-vertical form (THC = 59%) than in the *M*-horizontal form (THC = 61%).[48] The same situation is also found for the *P* form isomers: the *P*-horizontal form ($d_{\text{C28-S}} = 3.343$ Å, $\theta = 41.5°$, and THC = 63%) is more stable than the *P*-vertical form ($d_{\text{C28-S}} = 3.342$ Å, $\theta = 45.9°$, and THC = 60%) by 1.7 kcal mol^{-1}. When compared with the *M* form with the same N → B orientation (either horizontal or vertical), the *P* form encounters a larger steric hindrance but possesses a stronger N → B dative bond. The net effect seems determined by the steric effect, as the *P* form is predicted to be 2.3 kcal mol^{-1} higher in Gibbs free energy than the *M* form, consistent with the experimental observations. In the transition state (**TS**), the N → B dative bond is dissociated, enabling the boronate moiety to pass through the stator. Fig. 6c shows the free energy diagram of the *P* → *M* THI process. The DFT-derived barrier for the THI process from the *P*-

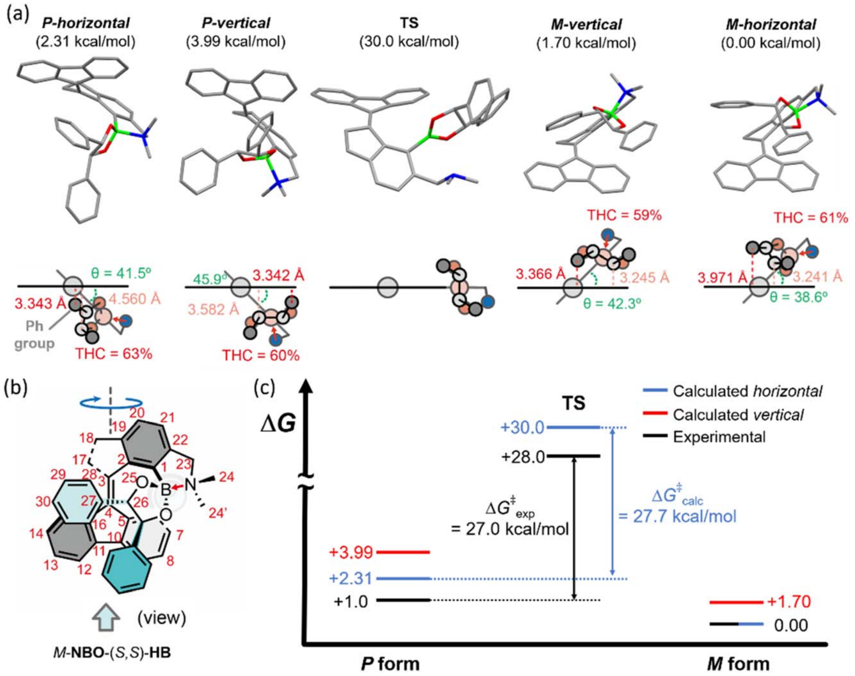

Fig. 6 (a) The DFT-optimized structures and pictorial representations of five representative conformations of NBO-(*S*,*S*)-HB. (b) The structure of *M*-NBO-(*S*,*S*)-HBthat shows the atomic numberings used for discussions. (c) The Gibbs free energy diagram of the *P* → *M* THI process for NBO-(*S*,*S*)-HB, where both the experimental and DFT-calculated values of the energy barrier are shown. The free energies (in kcal mol^{-1}) are referenced against the *M* form for experimental values and the *M*-horizontal form for the calculated values.

horizontal form is 27.7 kcal mol^{-1}, which agrees excellently with the experimentally determined 27.0 ± 0.9 kcal mol^{-1} (Fig. S10, S11 and Tables S5, S6†).

Upon retrieving the kinetic parameters above, the overall unidirectionality of the full rotation cycle for the **NBO-Diol** LRMMs warrants discussion. In principle, the unidirectionality of the light-driven rotation of LRMM is governed by the preference for PEZ over its thermal counterpart (TEZ), as well as for THI over the photochemical alternative (PHI). In the photochemical processes of **NBO-Diol** LRMMs, PEZ should consistently dominate due to its low energy barrier, a characteristic feature of sterically overcrowded stilbenes.[49] In contrast, PHI is unfavorable owing to its significantly higher energy barrier. Other potential competing processes, such as photolysis of the boronate moiety, are also unlikely, as they generally require short-wavelength excitation.[50,51] Even if such side reactions occur, they would affect only the rotational efficiency without perturbing the overall directionality. Regarding the thermal processes, direct characterization of the TEZ barrier is not feasible for the **NBO-Diol** LRMMs studied herein, since their C_2-symmetric stators preclude clear differentiation between the TEZ and THI pathways. Nevertheless, the TEZ barriers in overcrowded stilbenes rarely fall below 28.8 kcal mol^{-1},[52] which remains higher than the THI barrier determined for *M*-**NBO**-(*S*,*S*)-**HB** (27.7 kcal mol^{-1}), which is the highest among the **NBO-Diol** series. A recent example of an overcrowded stilbene with a lower TEZ barrier involves the incorporation of push–pull substituents *para* to the olefin bond, which reduces its bond order *via* enhanced charge-transfer character.[53] In the absence of such structural modifications, the TEZ barriers for the **NBO-Diol** LRMMs studied here should remain sufficiently higher than their THI barriers, rendering the impact of the TEZ pathway on overall rotational unidirectionality negligible. Therefore, it is reasonable to conclude that the **NBO-Diol** LRMMs exhibit net unidirectionality in their light-driven rotations, as the designated directionality is preserved across both the photochemical and thermal pathways that make up the full rotation cycle.

In addition, the role of the N → B dative bond in **NBO** was also investigated. We first optimized the crystal structure of *M*-**NBO**, which features intramolecular O–H⋯N hydrogen bonds, yielding a hydrogen-bonded conformer (**NBO**$_{\text{HB}}$, Fig. S12(a)†). Moreover, an N → B coordinated conformer (**NBO**$_{\text{N}\rightarrow\text{B}}$, Fig. S12(b)†) was derived from the optimized structure of *M*-**NBO**-(*S*,*S*)-**HB** by removing the **HB** moiety, followed by geometric re-optimization. The **NBO**$_{\text{HB}}$ conformer was found to be slightly more stable than **NBO**$_{\text{N}\rightarrow\text{B}}$ by 0.4 kcal mol^{-1}. We also evaluated interconversion between these two conformers by calculating the corresponding transition state (**NBO**$_{\text{TS}}$, Fig. S12(c)†), which predicted a small energy barrier of 7.65 kcal mol^{-1}. This suggests that both conformers coexist in equilibrium at room temperature, with an approximate **NBO**$_{\text{N}\rightarrow\text{B}}$ to **NBO**$_{\text{HB}}$ ratio of 1 : 2. In other words, only one-third of **NBO** molecules exhibit N → B coordination at room temperature, indicating a relatively weak N → B bond in **NBO**$_{\text{N}\rightarrow\text{B}}$. This conclusion is supported by the longer N → B bond length (1.774 Å *vs.* 1.686 Å) and lower THC (44% *vs.* 61%) at the boron center in **NBO**$_{\text{N}\rightarrow\text{B}}$ compared to *M*-**NBO**-(*S*,*S*)-**HB**. The observed upfield shift in the ^{11}B NMR signal upon formation of *M*-**NBO**-(*S*,*S*)-**HB** from **NBO** is also consistent with this analysis.

Direction-switching experiments of NBO-Diol motors

One of the strategies for switching the rotary direction of **NBO-Diol** motors is competitive diol exchange: namely, using diols with opposite helical preference for exchange (Fig. 7a). For example, diols with a high affinity for forming the boronate ester can displace the weakly bound diols (*e.g.*, (*S*,*S*)-**HB** *vs.* (*S*,*S*)-**DIPT**). In the case of two diols with similar binding affinities (*e.g.*, (*S*,*S*)-**BD** and (*S*,*S*)-**DIPT**), the one present at relatively high concentration would dominate the boronate ester formation. To demonstrate this strategy, we conducted an experiment involving sequential addition of chiral diols (*S*,*S*)-**BD**, (*S*,*S*)-**DIPT**, and (*S*,*S*)-**HB** into a solution of **NBO**, and monitored the process by ^{1}H NMR (Fig. 7b) and CD (Fig. 7c) spectroscopies. Similar to aforementioned experiments, the samples were heated after the addition of chiral diols to facilitate equilibration. The formation of the clockwise rotary motor **NBO**-(*S*,*S*)-**BD** was confirmed by the downfield and upfield shifts of the aromatic protons H$_6$ and H$_9$, respectively (Fig. 7b(i)). Then, 4.0 equivalents of (*S*,*S*)-**DIPT** were added to replace (*S*,*S*)-**BD** and generate the anticlockwise motor **NBO**-(*S*,*S*)-**DIPT**, accomplishing the first directionality switch (Fig. 7b(ii)). The second directionality switch followed by adding 3.0 equivalents of (*S*,*S*)-**HB** to replace (*S*,*S*)-**DIPT**, which led to the formation of the clockwise rotary motor **NBO**-(*S*,*S*)-**HB** (Fig. 7b(iii)). Note that the motor function of **NBO**-(*S*,*S*)-**HB** is not affected in the presence of free diols of opposite stereochemical configuration, such as (*S*,*S*)-**DIPT**. This is evidenced by an independent set of light-driven rotation experiment, in which the sample was prepared by adding 3.0 equivalents of (*S*,*S*)-**HB** into the CD_3CN solution of **NBO**-(*S*,*S*)-**DIPT** (Fig. S13†). These results demonstrate the feasibility of direction switching in EC-LRMMs such as the **NBO-Diol** systems.

Another strategy for switching the rotary direction in **NBO-Diol** motors is the recovery of the free receptor **NBO**, a resetting process, by removing the bound diol with a competing reagent (Fig. 7d). Once **NBO** is recovered, new chiral diols with different helical preference can be added to regenerate **NBO-Diol** motors with the opposite rotary direction. Solid-phase polystyrene-boronic acid (**PBA**) has been used for removing pinacol from pinacolyl boronate esters in acetonitrile solutions through transesterification and filtration.[54] The ability of **PBA** to extract the chiral diols from **NBO-Diol** motors and thus reset **NBO** has been demonstrated by the reaction of **NBO**-(*S*,*S*)-**HB** with 1.5 equivalents of HCl and 5.0 equivalents of **PBA** in 9 : 1 CD_3CN/D_2O. Since the amino group is protonated under acid conditions, the N → B dative bonding no longer exists, facilitating the removal of (*S*,*S*)-**HB** by **PBA**. Neutralization of the solution with 1.5 equivalents of NaOH is required to recover **NBO**. Following this resetting process, direction-switching can be achieved by adding one equivalent of (*R*,*R*)-**HB** to the solution. This results in the formation of the anticlockwise rotary motor **NBO**-(*R*,*R*)-

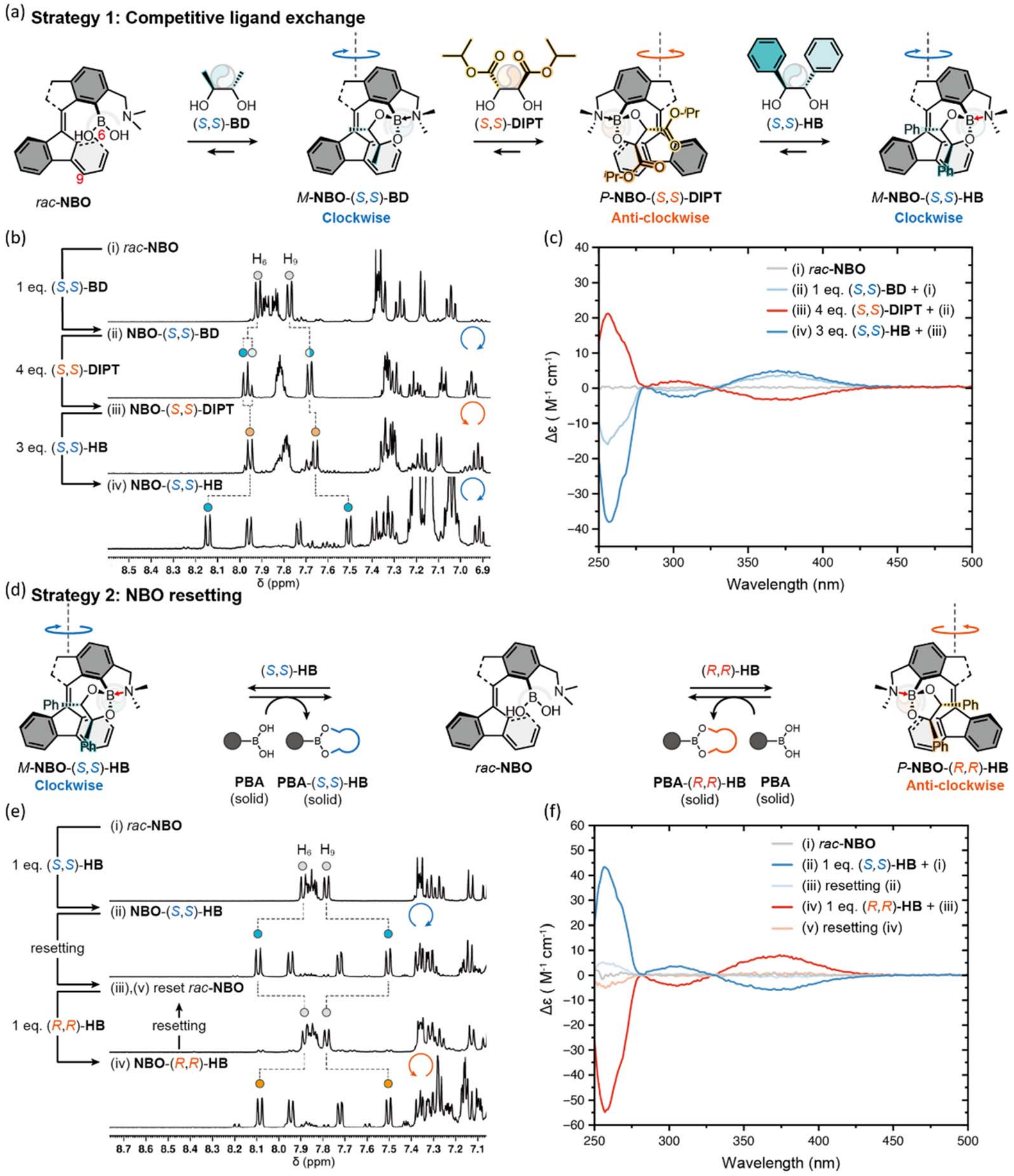

Fig. 7 Two strategies for directional switching of the **NBO-Diol** LRMMs. (a)–(c) The competitive ligand exchange strategy: conceptual representation (a), and spectral evolutions in ^1H NMR (400 MHz, CD_3CN) (b) and CD spectra (in acetonitrile) (c) of (i) **NBO** upon successive addition of (ii) (*S*,*S*)-**BD** (clockwise rotation), (iii) (*S*,*S*)-**DIPT** (anticlockwise rotation), and (iv) (*S*,*S*)-**HB** (clockwise rotation). (d)–(f) The **NBO** resetting strategy: conceptual representation (d), and spectral evolutions in ^1H NMR (400 MHz, $CD_3CN/D_2O = 9/1$) (e), and CD spectra (in acetonitrile) (f) of (i) **NBO** upon successive treatment of (ii) (*S*,*S*)-**HB** addition (clockwise rotation), (iii) resetting with **PBA**, (iv) (*R*,*R*)-**HB** addition (anticlockwise rotation), and (v) a repeat of step (iii) that recovers **NBO**. Procedure for **PBA** resetting: **PBA** (5.0 eq), $HCl_{(aq)}$ (1.5 eq) overnight, followed by filtration to remove the solids, and then adding $NaOH_{(aq)}$ (1.5 eq).

HB, as confirmed by the appearance of a new set of signals in the NMR spectrum (Fig. 7e) and the mirrored CD spectrum (Fig. 7f).

Conclusions

We have demonstrated the first example of dynamic covalent bonding-based LRMMs: the **NBO-Diol** systems. In these systems, the full 360° unidirectional rotation about the C=C bond can be switched from clockwise to anticlockwise, or *vice versa*, by altering the vicinal diol chirality through competitive diol exchange or **NBO** resetting methods. Similar to LRMMs based on intrinsic chirality, the rotation of **NBO-Diol** systems involves alternating photoisomerization and thermal helix inversion without requiring the dissociation of the external chiral diol. This work highlights dynamic covalent bonding as a powerful strategy for tuning the performance of artificial molecular machinery, offering enhanced precision and efficiency for targeted tasks.

Data availability

All experimental procedures and characterization data are available in the ESI.† CCDC 2294943 (**NBO**) and 2294942† (*M*-

NBO-(*S*,*S*)-**HB**) contain supplementary crystallographic data for this paper.

Author contributions

J.-S. Y. conceived the project. Z.-J. C. carried out the experiments. H.-F. L. and C.-P. H. performed theoretical calculations. Y.-H. L. did the crystallographic analysis. Z.-J. C., C.-W. C. and J.-S. Y. wrote, edited and completed the manuscript.

Conflicts of interest

The authors declare no conflicts of interest.

Acknowledgements

Financial support for this research was provided by the National Science and Technology Council of Taiwan (NSTC 110-2113-M-002-011-MY3; 113-2123-M-002-013) and National Taiwan University (NTU-113L892002). CPH acknowledgements support from Academia Sinica (AS-IV-114-M01), Academia Sinica Grid Computing Centre, (AS-CFII-114-A11), and National Science and Technology Council of Taiwan (NSTC 114-2811-M-001-015). We thank Dr Hsi-Ching Tseng at the NTU Instrumentation Center for the assistance in NMR experiments, and NTU Consortia of Key Technologies for the mass spectrometry technical research services.

References

1 Y. Feng, M. Ovalle, J. S. W. Seale, C. K. Lee, D. J. Kim, R. D. Astumian and J. F. Stoddart, *J. Am. Chem. Soc.*, 2021, **143**, 5569–5591.
2 V. García-López, D. Liu and J. M. Tour, *Chem. Rev.*, 2020, **120**, 79–124.
3 M. Baroncini, S. Silvi and A. Credi, *Chem. Rev.*, 2020, **120**, 200–268.
4 N. Koumura, R. W. J. Zijlstra, R. A. van Delden, N. Harada and B. L. Feringa, *Nature*, 1999, **401**, 152–155.
5 N. Koumura, E. M. Geertsema, A. Meetsma and B. L. Feringa, *J. Am. Chem. Soc.*, 2000, **122**, 12005–12006.
6 N. Ruangsupapichat, M. M. Pollard, S. R. Harutyunyan and B. L. Feringa, *Nat. Chem.*, 2011, **3**, 53–60.
7 P. Štacko, J. C. M. Kistemaker, T. van Leeuwen, M.-C. Chang, E. Otten and B. L. Feringa, *Science*, 2017, **356**, 964–968.
8 D. Roke, S. J. Wezenberg and B. L. Feringa, *Proc. Natl. Acad. Sci. U. S. A.*, 2018, **115**, 9423–9431.
9 S. J. Wezenberg and B. L. Feringa, *Nat. Commun.*, 2018, **9**, 1984.
10 J. C. M. Kistemaker, P. Štacko, J. Visser and B. L. Feringa, *Nat. Chem.*, 2015, **7**, 890–896.
11 L. Greb and J.-M. Lehn, *J. Am. Chem. Soc.*, 2014, **136**, 13114–13117.
12 L. Greb, A. Eichhöfer and J.-M. Lehn, *Angew. Chem., Int. Ed.*, 2015, **54**, 14345–14348.
13 M. Guentner, M. Schildhauer, S. Thumser, P. Mayer, D. Stephenson, P. J. Mayer and H. Dube, *Nat. Commun.*, 2015, **6**, 8406.
14 L. A. Huber, K. Hoffmann, S. Thumser, N. Böcher, P. Mayer and H. Dube, *Angew. Chem., Int. Ed.*, 2017, **56**, 14536–14539.
15 D. Roke, M. Sen, W. Danowski, S. J. Wezenberg and B. L. Feringa, *J. Am. Chem. Soc.*, 2019, **141**, 7622–7627.
16 K. Kuntze, D. R. S. Pooler, M. Di Donato, M. F. Hilbers, P. van der Meulen, W. J. Buma, A. Priimagi, B. L. Feringa and S. Crespi, *Chem. Sci.*, 2023, **14**, 8458–8465.
17 D. R. S. Pooler, A. S. Lubbe, S. Crespi and B. L. Feringa, *Chem. Sci.*, 2021, **12**, 14964–14986.
18 R. Eelkema, M. M. Pollard, J. Vicario, N. Katsonis, B. S. Ramon, C. W. M. Bastiaansen, D. J. Broer and B. L. Feringa, *Nature*, 2006, **440**, 163.
19 D. Daou, Y. Zarate, M. Maaloum, D. Collin, G. Fleith, D. Constantin, E. Moulin and N. Giuseppone, *Adv. Mater.*, 2024, **36**, 2311293.
20 Y. Qutbuddin, A. Guinart, S. Gavrilović, K. Al Nahas, B. L. Feringa and P. Schwille, *Adv. Mater.*, 2024, **36**, 2311176.
21 M. Kathan, S. Crespi, N. O. Thiel, D. L. Stares, D. Morsa, J. de Boer, G. Pacella, T. van den Enk, P. Kobauri, G. Portale, C. A. Schalley and B. L. Feringa, *Nat. Nanotechnol.*, 2022, **17**, 159–165.
22 V. García-López, F. Chen, L. G. Nilewski, G. Duret, A. Aliyan, A. B. Kolomeisky, J. T. Robinson, G. Wang, R. Pal and J. M. Tour, *Nature*, 2017, **548**, 567–572.
23 A. Guinart, M. Korpidou, D. Doellerer, G. Pacella, M. C. A. Stuart, I. A. Dinu, G. Portale, C. Palivan and B. L. Feringa, *Proc. Natl. Acad. Sci. U. S. A.*, 2023, **120**, e2301279120.
24 B. B. Berking, S. J. Rijpkema, B. H. E. Zhang, A. Sait, H. Amatdjais-Groenen and D. A. Wilson, *ACS Biomater. Sci. Eng.*, 2024, **10**, 5881–5891.
25 S. Deng, Z. Li, L. Yuan, J. Shen and H. Zeng, *Nano Lett.*, 2024, **24**, 10750–10758.
26 J. Chen, F. K.-C. Leung, M. C. A. Stuart, T. Kajitani, T. Fukushima, E. van der Giessen and B. L. Feringa, *Nat. Chem.*, 2018, **10**, 132–138.
27 X. Yao, J. A. Vishnu, C. Lupfer, D. Hoenders, O. Skarsetz, W. Chen, D. Dattler, A. Perrot, W.-z. Wang, C. Gao, N. Giuseppone, F. Schmid and A. Walther, *Adv. Mater.*, 2024, **36**, 2403514.
28 A. Perrot, W.-z. Wang, E. Buhler, E. Moulin and N. Giuseppone, *Angew. Chem., Int. Ed.*, 2023, **62**, e202300263.
29 Q. Li, G. Fuks, E. Moulin, M. Maaloum, M. Rawiso, I. Kulic, J. T. Foy and N. Giuseppone, *Nat. Nanotechnol.*, 2015, **10**, 161–165.
30 A. Ryabchun, F. Lancia, J. Chen, R. Plamont, D. Morozov, B. L. Feringa and N. Katsonis, *Chem*, 2023, **9**, 3544–3554.
31 Q. Zhou, J. Chen, Y. Luan, P. A. Vainikka, S. Thallmair, S. J. Marrink, B. L. Feringa and P. van Rijn, *Sci. Adv.*, 2020, **6**, eaay2756.
32 D. J. DeRosier, *Cell*, 1998, **93**, 17–20.
33 K. Kinosita, R. Yasuda, H. Noji, S. i. Ishiwata and M. Yoshida, *Cell*, 1998, **93**, 21–24.

34 L. Reißenweber, E. Uhl, F. Hampel, P. Mayer and H. Dube, *J. Am. Chem. Soc.*, 2024, **146**, 23387–23397.

35 S. Borsley, E. Kreidt, D. A. Leigh and B. M. W. Roberts, *Nature*, 2022, **604**, 80–85.

36 S. Chatterjee, E. V. Anslyn and A. Bandyopadhyay, *Chem. Sci.*, 2021, **12**, 1585–1599.

37 Y. Kubo, R. Nishiyabu and T. D. James, *Chem. Commun.*, 2015, **51**, 2005–2020.

38 S. D. Bull, M. G. Davidson, J. M. H. van den Elsen, J. S. Fossey, A. T. A. Jenkins, Y.-B. Jiang, Y. Kubo, F. Marken, K. Sakurai, J. Zhao and T. D. James, *Acc. Chem. Res.*, 2013, **46**, 312–326.

39 X. Sun, B. M. Chapin, P. Metola, B. Collins, B. Wang, T. D. James and E. V. Anslyn, *Nat. Chem.*, 2019, **11**, 768–778.

40 Z.-J. Chen, H.-F. Lu, I. Chao and J.-S. Yang, *J. Org. Chem.*, 2022, **87**, 5029–5034.

41 Z.-J. Chen, H.-F. Lu, I. Chao and J.-S. Yang, *J. Chin. Chem. Soc.*, 2022, **69**, 1475–1484.

42 Z.-J. Chen, H.-F. Lu, C.-W. Chiu, F.-M. Hou, Y. Matsunaga, I. Chao and J.-S. Yang, *Org. Lett.*, 2020, **22**, 9158–9162.

43 S. F. Pizzolato, P. Štacko, J. C. M. Kistemaker, T. van Leeuwen, E. Otten and B. L. Feringa, *J. Am. Chem. Soc.*, 2018, **140**, 17278–17289.

44 S. A. Valenzuela, J. R. Howard, H. M. Park, S. Darbha and E. V. Anslyn, *J. Org. Chem.*, 2022, **87**, 15071–15076.

45 R. A. Brown, V. Diemer, S. J. Webb and J. Clayden, *Nat. Chem.*, 2013, **5**, 853–860.

46 A. V. Marenich, C. J. Cramer and D. G. Truhlar, *J. Phys. Chem. B*, 2009, **113**, 6378–6396.

47 M. J. Frisch, G. W. Trucks, H. B. Schlegel, G. E. Scuseria, M. A. Robb, J. R. Cheeseman, G. Scalmani, V. Barone, B. Mennucci, G. A. Petersson, H. Nakatsuji, M. Caricato, X. Li, H. P. Hratchian, A. F. Izmaylov, J. Bloino, G. Zheng, J. L. Sonnenberg, M. Hada, M. Ehara, K. Toyota, R. Fukuda, J. Hasegawa, M. Ishida, T. Nakajima, Y. Honda, O. Kitao, H. Nakai, T. Vreven, J. A. Montgomery Jr, J. E. Peralta, F. Ogliaro, M. Bearpark, J. J. Heyd, E. Brothers, K. N. Kudin, V. N. Staroverov, R. Kobayashi, J. Normand, K. Raghavachari, A. Rendell, J. C. Burant, S. S. Iyengar, J. Tomasi, M. Cossi, N. Rega, J. M. Millam, M. Klene, J. E. Knox, J. B. Cross, V. Bakken, C. Adamo, J. Jaramillo, R. Gomperts, R. E. Stratmann, O. Yazyev, A. J. Austin, R. Cammi, C. Pomelli, J. W. Ochterski, R. L. Martin, K. Morokuma, V. G. Zakrzewski, G. A. Voth, P. Salvador, J. J. Dannenberg, S. Dapprich, A. D. Daniels, O. Farkas, J. B. Foresman, J. V. Ortiz, J. Cioslowski and D. J. Fox, *Gaussian 09*, 2009.

48 H. Höpfl, *J. Organomet. Chem.*, 1999, **581**, 129–149.

49 M. Quick, F. Berndt, A. L. Dobryakov, I. N. Ioffe, A. A. Granovsky, C. Knie, R. Mahrwald, D. Lenoir, N. P. Ernsting and S. A. Kovalenko, *J. Phys. Chem. B*, 2014, **118**, 1389–1402.

50 R. F. Porter and L. J. Turbini, *Photochemistry of Boron Compounds*, Springer, Berlin, 1981.

51 A. Pelter, R. T. Pardasani and P. Pardasani, *Tetrahedron*, 2000, **56**, 7339–7369.

52 J. C. M. Kistemaker, S. F. Pizzolato, T. van Leeuwen, T. C. Pijper and B. L. Feringa, *Chem. Eur. J.*, 2016, **22**, 13478–13487.

53 L. Pfeifer, S. Crespi, P. van der Meulen, J. Kemmink, R. M. Scheek, M. F. Hilbers, W. J. Buma and B. L. Feringa, *Nat. Commun.*, 2022, **13**, 2124.

54 T. E. Pennington, C. Kardiman and C. A. Hutton, *Tetrahedron Lett.*, 2004, **45**, 6657–6660.